Title

Corrigendum: Carbon nanotube thin film strain sensors: comparison between experimental tests and numerical simulations (2017 *Nanotechnology* **28** 155502)

Journal

Nanotechnology, 30(43)

ISSN

0957-4484

Authors

Lee, Bo Mi
Loh, Kenneth J

Publication Date

2019-10-25

DOI

10.1088/1361-6528/ab3696

Peer reviewed

Carbon nanotube thin film strain sensors: comparison between experimental tests and numerical simulations

Bo Mi Lee[1] and Kenneth J. Loh[1,*]
[1] Department of Structural Engineering, University of California-San Diego, La Jolla, CA 92093-0085, USA

[*]E-mail: kenloh@ucsd.edu

Abstract. Carbon nanotubes can be randomly deposited in polymer thin film matrices to form nanocomposite strain sensors. However, a computational framework that enables the direct design of these nanocomposite thin films is still lacking. The objective of this study is to derive an experimentally validated and 2D numerical model of carbon nanotube-based thin film strain sensors. This study consisted of two parts. First, multi-walled carbon nanotube (MWCNT)-Pluronic strain sensors were fabricated using vacuum filtration, and their physical, electrical, and electromechanical properties were evaluated. Second, scanning electron microscope images of the films were used for identifying topological features of the percolated MWCNT network, where the information obtained was then utilized for developing the numerical model. Validation of the numerical model was achieved by ensuring that the area ratios (of MWCNTs relative to the polymer matrix) were equivalent for both the experimental and modeled cases. Strain sensing behavior of the percolation-based model was simulated and then compared to experimental test results.

Keywords: carbon nanotube, electromechanical property, multi-walled carbon nanotube, nanocomposite, strain sensor, scanning electron microscopy, thin film

1. Introduction

Nanomaterials are defined as materials in which at least one of its dimensions is less than 100 nm. They can be categorized as zero-dimensional (*e.g.*, nanoparticles [1]), one-dimensional (1D) (*e.g.*, nanowires [2] and nanotubes [3]), two-dimensional (2D) (*e.g.*, graphene [4]), and three-dimensional (3D) (*e.g.*, box-shaped graphene [5]). Their unique nanostructure and high surface area-to-volume ratio allow them to possess outstanding electrical [6], optical [7], and magnetic properties that can be drastically different than their bulk material counterparts [8]. For instance, carbon nanotubes (CNT) are characterized by extremely high length-to-diameter ratios (*i.e.*, aspect ratio) of up to 4,000 [9]. They are classified as single-walled carbon nanotubes (SWCNT) in which they physically represent a rolled graphene sheet, whereas multi-walled carbon nanotubes (MWCNT) consist of multiple layers of concentrically stacked nanotubes of different diameters. The 1D morphology of CNTs allows near-ballistic electron transport in metallic CNTs with minimal scattering, leading to relatively high conductivity [10]. For example, Ebbesen *et al.* [11] found through experiments that the conductivity of MWCNTs was on the order of 10^5 to 10^6 S/m. On the other hand, their carbon-carbon covalent bonds directly contribute to their impressive mechanical properties (*i.e.*, high stiffness and strength) [6]. Treacy *et al.* [12] estimated the Young's moduli of 11 different isolated MWCNTs to be between 0.40 to 4.15 TPa, with an average value of 1.8 TPa. On the other hand, Yu *et al.* [13] found that the tensile strength of MWCNTs can be as high as 63 GPa. Furthermore, the electrical properties of CNTs respond to applied mechanical stimuli. It was found that conductance of an SWCNT decreased by two orders of magnitude when it was strained using an atomic force microscope (AFM) tip using a three-point bending test setup [14].

The unique intrinsic nano-scale properties of CNTs can be translated to larger length scales by dispersing and incorporating them in polymer matrices to form nanocomposite thin films. Many had explored this strategy for enhancing the mechanical [15, 16], electrical [17-19], and thermal properties [20] of CNT-based nanocomposites. To be specific, Ruan *et al.* [15] dispersed 1 *wt.*% MWCNTs in a polyethylene matrix, and the tensile strength of the nanocomposite improved by 49.7%. When 0.5 *wt.*% amino-functionalized double-walled nanotubes (DWNT-NH_2) were dispersed in epoxy, Gojny *et al.* [16] reported that the nanocomposite's strength, stiffness, and fracture toughness increased by 10%, 15%, and 43%, respectively. In addition, Biercuk *et al.* [20] showed that the thermal conductivity of 1 *wt.*% SWCNT-epoxy composites improved by 70% at 40 K and 125% at room temperature. On the other hand, polymer thin films can be made conductive by incorporating CNTs, particularly, at low concentrations if high-aspect-ratio nanotubes are employed. For example, Kim *et al.* [17] found that the percolation threshold of oxidized MWCNT-polyurethane composites was 0.018 *wt.*%. Similarly, Sandler *et al.* [18] and Martin *et al.* [19] found that the percolation thresholds of MWCNT-epoxy nanocomposites were 0.0025 *wt.*% and 0.0021 *wt.*%, respectively.

Another advantage of CNT-based nanocomposites is that its electrical resistance can change when subjected to applied strains and deformations, thereby making them ideal strain sensors [21, 22]. Since the percolated nanotube network is responsible for conducting electricity, any changes to this network (*i.e.*, due to strain) would alter its bulk conductivity and resistivity. Thus, novel strain sensors fabricated using various techniques were investigated [23-30]. Recently, Zhang *et al.* [24] fabricated SWCNT buckypapers infiltrated with epoxy resin. It was demonstrated that nonlinear and unstable piezoresistive response with relatively low strain sensitivity (<4) was detected at low strains ($\varepsilon < 2{,}000\ \mu\varepsilon$), while linear piezoresistivity with higher strain sensitivity (~6.2) was observed at high strains ($2{,}000\ \mu\varepsilon < \varepsilon < 10{,}000\ \mu\varepsilon$). Layer-by-Layer assembly is another technique for fabricating mechanically strong and homogeneous CNT-based strain sensors. For example, Loh *et al.* [25] assembled homogeneous, multilayered, CNT-polyelectrolyte (PE) thin films by successively dipping glass substrates in a polycationic solution and polyanionic CNT suspension. Load tests revealed that the resistance of CNT-PE thin film varied in tandem with applied tensile-compressive cyclic loading. Kang *et al.* [27] employed *in situ* polymerization under sonication and mechanical shear to build SWCNT-polyimide thin films and studied the strain sensitivity of films with different SWCNT concentrations. The optimal strain sensing properties corresponded to nanocomposites

with 0.05 *wt.*% SWCNTs, which was just slightly higher than its percolation threshold of ~0.04 *wt.*%. These aforementioned examples showcase the different methods commonly used for strain sensor fabrication, but it should be noted that other fabrication techniques have also been used, such as spin coating [28], dip coating [31], and inkjet printing [30], among others [32]. The choice to adopt certain fabrication methods is dictated by nanocomposite constituents and the thin film's intended applications [23].

Although CNT-based strain sensors can be designed to possess unique properties (*e.g.*, high sensitivity), their piezoresistivity is affected by CNTs' intrinsic characteristics (*e.g.*, length [33], type [34], and alignment [35]) and other extrinsic properties such as the polymer matrix [36], fabrication procedure [23], curing temperature [26], and sonication [29]. As a result, analytical methods were used to better understand the relationship between the nano-scale features of thin film constituents and their bulk electrical and electromechanical properties. For example, Hu *et al.* [37] modeled nanotubes as soft-core cylinders dispersed in a cubic space to study the electrical and piezoresistive response of the model. Tunneling between neighboring nanotubes was considered as the main mechanism for enabling nanocomposite piezoresistivity, while intrinsic CNT piezoresistivity and CNT-to-CNT contact resistance were not considered. When the CNT-based nanocomposite model was subjected to uniaxial tensile strains to 7,000 με, nonlinear strain sensing response was observed. Similarly, Rahman *et al.* [38] simulated strain sensing response of a network of nanotubes modeled as straight elements while considering tunneling resistance. Linear piezoresistivity was observed during small strains ($\varepsilon < 0.01$), but nonlinearity was observed at higher strains ($0.2 < \varepsilon < 1.5$). In addition, lower strain sensitivity was found when nanotubes were randomly dispersed as compared to an aligned nanotube network, which was inconsistent with results reported by Hu *et al.* [29]. On the other hand, Wang *et al.* [39] employed average junction gap variation (AJGV), which is an average of the distances between the surfaces of two adjacent nanotubes, to describe electrical properties of nanotube-polymer composites. It was proposed that the piezoresistivity of nanocomposites can be enhanced by maximizing AJGV with large nanotube diameter, lower nanotube concentration, and low Poisson's ratio of the polymer matrix. Amini *et al.* [40] employed graph conductance theory, where the algorithm looked for the shortest path between two end-electrodes to calculate the bulk electrical properties of the model. The results showed that higher strain sensitivity was observed near the percolation threshold. Recently, Lee *et al.* [41] developed a 2D percolation-based CNT thin film model to study how variations in nanotube parameters (*i.e.*, density, length, and intrinsic piezoresistivity) affected bulk film electromechanical properties. It was found that the inherent piezoresistivity of nanotubes was correlated with bulk film strain sensitivity. In addition, strain sensitivity decreased as CNT density increased [29, 40], although an inconsistent trend was observed near percolation.

Despite these extensive experimental and numerical studies on CNT-based strain sensors, the integration of the two are limited. With the exception of a few studies [29, 37], most studies focused solely on experiments [24-28, 30, 42] or numerical simulations [28, 38-41]. Therefore, the objective of this study was to characterize the strain sensing properties of MWCNT-Pluronic® nanocomposites, both experimentally and using a 2D percolation-based numerical model. The aim was to understand the underlying mechanisms that contribute to the strain sensing properties of MWCNT-Pluronic nanocomposites. This study first began with the fabrication of MWCNT-Pluronic nanocomposites using a vacuum filtration method. Second, the films were subjected to uniaxial tensile strains while their electrical properties were measured, so as to characterize their strain sensing properties. Third, an experimentally validated, 2D, percolation-based, numerical model of the film was built with inputs obtained from scanning electron microscope (SEM) images of the fabricated films (*i.e.*, physical properties of CNTs as-deposited in the film). Then, the numerical models were subjected to the same tensile strain patterns, and the electromechanical properties of the model were compared with the experimental results.

2. Experimental methods

2.1. Materials

MWCNT (outer diameter: 10 nm, median length: 3 μm, and purity > 98%) and Pluronic® F-127 (Pluronic) ($M_W \approx 12{,}600$) were acquired from Sigma-Aldrich. Hydrophilic polytetrafluoroethylene (PTFE) membrane filters (diameter: 47 mm and pore size: 0.45 μm) were purchased from EMD Millipore.

2.2. Nanocomposite fabrication

MWCNT-Pluronic buckypaper specimens were fabricated using vacuum filtration (figure 1) [24, 42]. An advantage of using vacuum filtration is that the density of film constituents (*i.e.*, nanotubes and polymers) can be precisely controlled. First, 1 *wt.*% Pluronic solution was prepared by dissolving Pluronic powder in deionized (DI) water. Pluronic is a triblock copolymer with a central propylene oxide block and ethylene oxide chains, both of which are water soluble. Because of its amphiphilic characteristic, Pluronic can disperse nanotubes in aqueous solutions and achieving steric stabilization, which prevents agglomeration of nanotubes [43]. Shvartzman-Cohen *et al.* [44] demonstrated that SWCNTs can be dispersed in Pluronic solution well below the critical micellar concentration and critical micellar temperature. Zhao *et al.* [36] found that MWCNT-Pluronic dispersions remained stable for weeks. Thus, to attain homogeneous dissolution, the mixture was constantly stirred using a magnetic stirrer (Corning) at 55 °C for ~90 min. Second, upon stirring and when the Pluronic solution cooled to room temperature, dispersion of MWCNTs was achieved by subjecting MWCNT-Pluronic mixtures to 60 min of high-energy tip sonication (3 mm tip, 150 W, 22 kHz) [36]. In this study, seven different concentrations of MWCNT-Pluronic solution were prepared, namely 0.25, 0.5, 1, 2, 3, 4, and 5 mg/mL, to quantify the effects of MWCNT concentration on the strain sensing behavior of MWCNT-Pluronic nanocomposites. Next, the stable suspension was vacuum-filtered using a PTFE membrane. Finally, the film, together with the membrane filter, was dried for 12 h at 60 °C in a StableTemp vacuum oven. Figure 1 shows a picture of an MWCNT-Pluronic buckypaper specimen still attached to its PTFE filtration membrane.

2.3. Strain sensing characterization

The strain sensing properties of MWCNT-Pluronic buckypaper were characterized by applying uniaxial tensile cyclic strains to the films while simultaneously measuring their change in electrical properties. First,

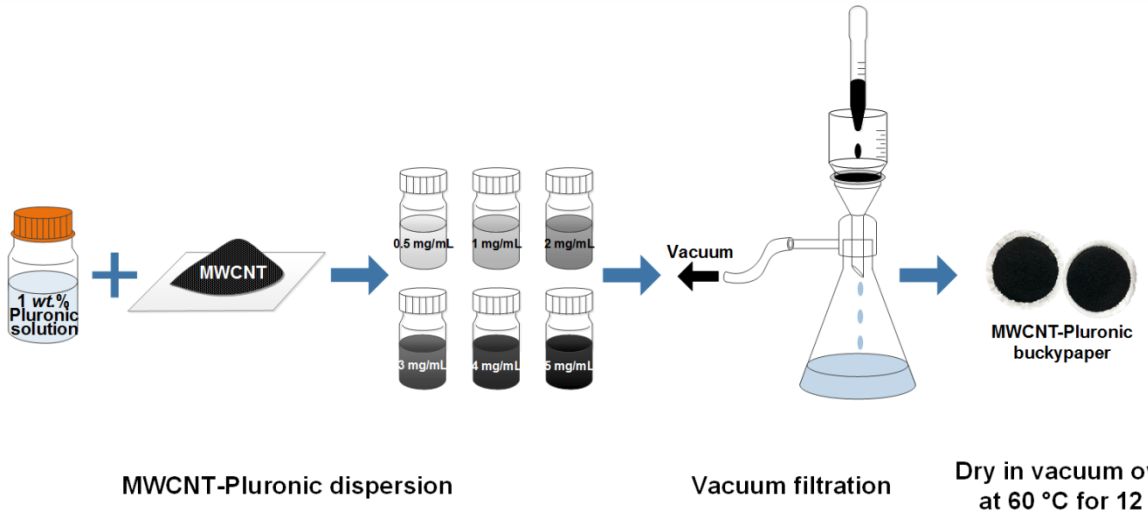

Figure 1. An MWCNT-Pluronic buckypaper was fabricated, first, by dispersing MWCNTs in 1 *wt.*% Pluronic solution. Then, the solution was vacuum filtered using PTFE membrane filter (pore size: 0.45 μm) and dried in a vacuum oven at 60 °C for 12 h.

MWCNT-Pluronic buckypaper that was still attached to its PTFE membrane was cut to form smaller specimens of 4×30 mm^2. Second, two electrodes were established at opposite ends of the specimen using 1.5 mm-wide copper tape strips for two-point probe electrical measurements during load testing. Silver paste (Ted Pella) was applied over the copper tape electrodes and film for minimizing contact impedance and then dried in air for ~3 h. The distance between two electrodes (*i.e.*, gage length) was ~24 mm.

MWCNT-Pluronic buckypaper specimens were then subjected to electromechanical testing using a Test Resources 150R load frame with a 4.89 N (1.1. lbf) load cell installed (figure 2). To ensure that the specimen is flat and taut, the load frame applied a preload to 0.2 N. Then, the load frame executed a five-cycle uniaxial tensile load pattern to strain the film to a maximum strain of 2,500 με (load rate: 5,000 με/min). Throughout the entire test, an Agilent 34401A digital multimeter recorded the electrical resistance of the film. The load frame's cross-head displacement, applied load, and the multimeter's electrical resistance measurements were simultaneously collected using a customized LabVIEW program. It should be mentioned that, since nanotubes are sensitive to environmental stimuli (*e.g.*, temperature [45], light [46], and humidity [47]), these tests were performed by shielding the entire test setup with a blackout curtain.

3. Numerical simulation methods

3.1. Morphology characterization and model generation

As an effort to understand and explain the experimental results of MWCNT-Pluronic strain sensor, a 2D CNT-based nanocomposite model was developed. Previous studies derived a 2D percolation-based model assuming that the CNTs were straight [41]. While the thin film model was able to explain how different parameters (*i.e.*, length, density, and intrinsic piezoresistivity of nanotubes) were correlated to bulk film electrical and electromechanical properties, other studies reported that the geometry of nanotubes would affect bulk film properties as well [48-50]. For example, Yi *et al.* [50] compared the percolation threshold of 2D fibrous networks with different geometries of conductive fibers (*i.e.*, rectangle, sinusoidal, and kinked fibers). The author concluded that the curl ratio significantly affected percolation threshold (*i.e.*, percolation threshold increased with higher curl ratio), whereas percolation threshold was not affected by fiber geometries (*i.e.*, sinusoid, triangle, and rectangle) of identical curl ratio. Li *et al.* [51] defined the effective nanotube length as the maximum distance between two arbitrary points on the nanotube. It was demonstrated that higher curl ratio decreased the electrical conductivity of the nanocomposite. Dalmas *et*

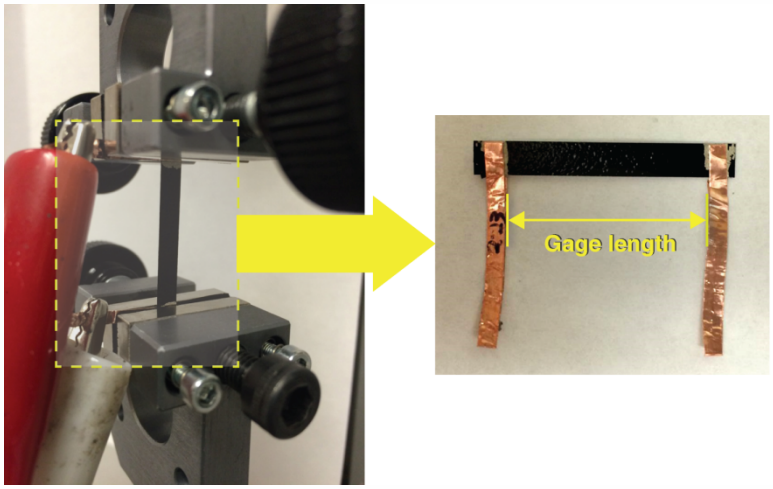

Figure 2. An MWCNT-Pluronic strain sensor was mounted in a Test Resources 150R load frame for strain sensing characterization.

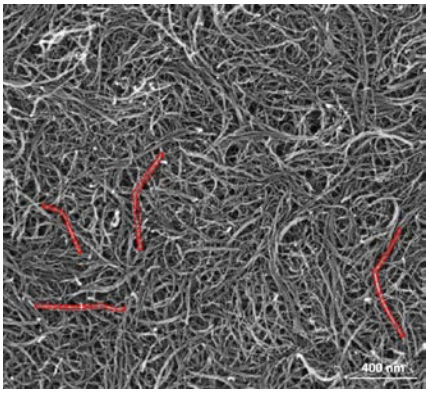

Figure 3. An SEM image of a 2 mg/mL MWCNT-Pluronic buckypaper shows the random, percolated morphology of MWCNTs.

al. [48] numerically showed that increasing the tortuosity of CNTs in a 3D fibrous network increased percolation threshold. Berhan *et al.* [52] demonstrated that the effect of the shape of CNTs on percolation threshold increased when its aspect ratio was less than 1,000.

In order to develop models that more accurately represented the actual shapes of CNTs in the thin film, SEM imaging was used to characterize the morphology of nanotubes in MWCNT-Pluronic buckypapers. Using an FEI 230 NanoSEM, one can obtain SEM images of the thin film, such as that shown in figure 3, which clearly shows that MWCNTs were randomly oriented to form a densely percolated network. Although it is hard to locate the end-points of each nanotube, figure 3 shows that MWCNTs were curved or slightly kinked. For instance, most nanotubes physically represent a half-cycle sinusoidal shape. Therefore, based on this observation, a 2D nanocomposite model can be generated. Here, the dimensions of the model (*i.e.*, length, L, and width, W) were set as 4×24 μm^2 to have the same aspect ratio (*i.e.*, 1:6) as the MWCNT-Pluronic thin films in Section 2. It should be noted that the numerical model was developed specific to the type of film fabricated in this study, and changes to fabrication procedure and the type of nanotubes used, among others, could change the results; nevertheless, the procedure for model generation employed in this study would still apply.

Before generating the CNTs in the model space, the physical properties of the as-deposited MWCNTs were needed. In a previous study [53], atomic force microscopy (AFM) was performed on 1 μg/mL MWCNT-poly(sodium 4-styrenesulfonate) thin films. AFM images of individual MWCNTs (which were the same types used in this work) were obtained, and the lengths of 20 MWCNTs were measured by image analysis. The results showed that the distribution of MWCNT lengths followed a Gaussian distribution with a mean and standard deviation of 1.904 μm and 0.506 μm, respectively [53]. Using this statistical information, N number of MWCNTs (or equivalently related to density) were populated in the model space using MATLAB's random number generator, *normrnd*. The shape of MWCNTs were assumed to be kinked as a simplified representation of the half-cycle sinusoidal shapes observed in figure 3. To decrease computational demand, the kinked shape comprised of two equidistant linear segments ($L_{CNT}/2$), where L_{CNT} is the total nanotube length. The position of the MWCNTs within the model space was also randomly determined, and one end of the MWCNT (at x_1, y_1) was defined by a distance (l_i) and orientation angle (α_i) with respect to the origin (0, 0) in a Cartesian coordinate system (figure 4). To describe the degree of nanotube kink, a height ratio can also be defined as follows:

$$HR = \frac{H_{CNT}}{L_{CNT}} \tag{1}$$

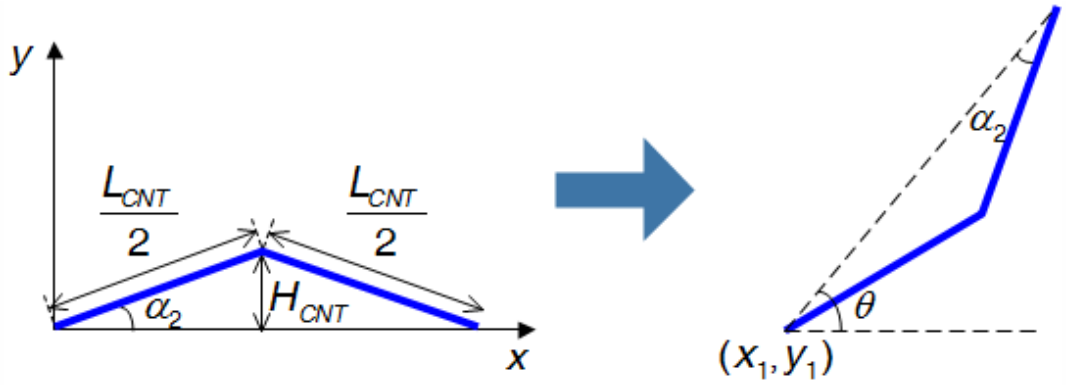

Figure 4. A kinked CNT can be described by the ratio of height-to-length of CNT (*i.e.*, height ratio or *HR*).

where H_{CNT} is the distance from the vertex of the MWCNT relative to its local x-axis that intersects its two end-points (figure 4). In this study, four different height ratios (*i.e.*, 0, 10, 20, and 30%) were considered. Once each MWCNT was generated and its first end-point positioned at (x_1, y_1), the other two points (*i.e.*, vertex and end-point) were determined using α_i and a random rotation angle (θ):

$$\begin{aligned} x_i &= x_1 + l_i \cos(\theta - \alpha_i) \\ y_i &= y_1 + l_i \sin(\theta - \alpha_i) \end{aligned} \tag{2}$$

This procedure allowed the generation of one nanotube, which was then iterated until the predetermined number of CNTs (N) was populated in the 4×24 μm^2 representative area. Periodic boundary conditions were applied to the model to ensure that CNT density remained constant based on N. A representative numerical model with N = 400 and HR = 20% is shown in figure 5 as an example. Similar to the MWCNT-Pluronic thin films in Section 2, the top and bottom boundaries of the model were assumed as the conductive electrodes.

3.2. Strain sensing simulation

The strain sensing behavior of the CNT-based nanocomposite model was simulated by calculating the electrical resistance of the model at different strain states. Evaluation of the electrical properties was performed by considering the randomly distributed CNTs (*i.e.*, conductor) as an equivalent conductor or resistor network [37]. The details of the procedure are reported in a previous study [54] but are briefly summarized here. First, the algorithm started by searching for locations of nanotube-to-nanotube junctions between two CNTs. Junction locations and the corresponding segment numbers were stored in a matrix, which was then used to calculate element resistance followed by nodal voltage analysis. Element resistance was calculated using:

$$R = R_{int} + R_{jct} + R_{Ohmic} \tag{3}$$

where R_{int} is the intrinsic resistance of a CNT assuming perfect contact (*i.e.*, R_{int} = 6.5 kΩ), R_{jct} is additional contact resistance due to imperfect contact, and R_{Ohmic} is Ohmic resistance caused by carrier scattering due to defects, impurities, and phonons [55]. Here, Ohmic resistance depends on the length of the resistor or conductor (*i.e.*, junction-to-junction length). It should be mentioned that this model does not distinguish between SWCNTs and MWCNTs. In addition, even though the electrical characteristics of a junction varies depending on SWCNT chirality (*i.e.*, whether they are metallic or semiconducting) and the intersection of two different types of nanotubes to form the junction [56], R_{jct} was assumed to be 240 kΩ specific to metal-

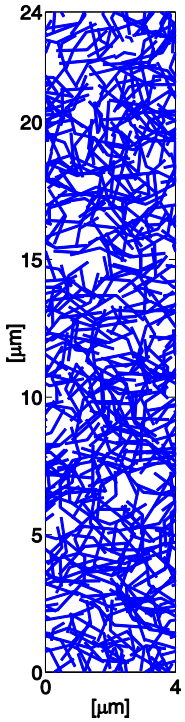

Figure 5. A representative nanocomposite model shows that kinked CNTs are randomly distributed in a 4×24 μm^2 area (N = 400 and HR = 20%).

metal junction resistance [57]. The reciprocal of the calculated element resistance was used to construct a conductance matrix of the entire CNT network. Upon doing so, Kirchhoff's current law and the conductance version of Ohm's law were applied to determine nodal voltage. The total current propagating through the nanocomposite model was determined using the nodal voltage and element resistance connected to the drain (*i.e.*, bottom boundary of the model). Finally, the resistance of the entire CNT network can be computed using the total current and applied voltage between the source (*i.e.*, top electrode) and drain. This procedure was executed prior to straining the model to determine its nominal or unstrained electrical resistance.

Then, the model was subjected to uniaxial tensile and compressive strains, and the coordinates of each CNT in the network were updated, assuming that mechanical strain was applied uniformly to the entire nanocomposite. The new coordinates of each strained nanotube (x', y') are:

$$\begin{aligned} x' &= x - \nu\left(x - \frac{W}{2}\right) \\ y' &= y(1+\varepsilon) \end{aligned} \tag{4}$$

where x and y are the unstrained initial coordinates of the CNT, ν is Poisson's ratio of the polymer matrix, and ε is applied strain. Once the coordinates of all the CNTs were updated, the element resistance and electrical resistance of the deformed CNT network were recalculated. It should be mentioned that, in this work, intrinsic strain sensitivity (S_{CNT}) of CNTs was also incorporated to the model and assumed to be 150 [58]. Finally, after calculating the models' electrical resistances corresponding to different strain states, their strain sensing properties were evaluated.

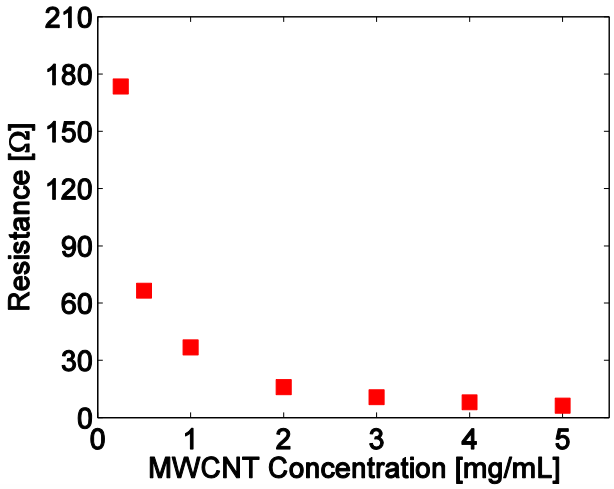

Figure 6. The unstrained electrical resistances of MWCNT-Pluronic strain sensors are plotted as a function of MWCNT concentration.

4. Experimental results

The electrical properties and strain sensing behavior of MWCNT-Pluronic nanocomposites were characterized by following the procedures described in Section 2.3. The nominal or unstrained electrical resistance measurements are plotted in figure 6. For each MWCNT concentration, 10 nominal resistance measurements were obtained and then averaged. It can be seen from figure 6 that the electrical resistance of the buckypaper decreased with increasing MWCNT concentrations. This result is expected, since higher densities of MWCNTs create denser networks of electrical conducting pathways, which result in higher bulk electrical conductance and lower electrical resistance. However, the rate of decrease in resistance with increasing MWCNT concentrations was nonlinear and slowed down. To be specific, when MWCNT concentration increased from 1 to 2 mg/mL, resistance decreased from 36.82 to 15.94 kΩ (*i.e.*, 56.7% decrease); from 4 to 5 mg/mL, resistance decreased from 8.03 to 6.28 kΩ (*i.e.*, 21.8% decrease).

In addition, the strain sensing properties of MWCNT-Pluronic nanocomposite were characterized. In a previous study, the electrical resistance of MWCNT-latex thin films deposited on polyethylene terephthalate substrates exhibited linear piezoresistivity in response to applied tensile cyclic loading [59]. Similarly, when MWCNT-Pluronic strain sensors were subjected to five-cycle, uniaxial, tensile strains, their electrical resistance varied in tandem with applied strains. The results are summarized in figure 7. In figure 7(a)-(c), the electrical resistance time histories of three films with different MWCNT concentrations were overlaid with their corresponding applied cyclic load pattern. Here, only the responses from the second to fifth cycles are shown, and the first-cycle data was omitted; most specimens showed relatively higher increases in resistance during initial loading, which could be due to permanent deformation in the PTFE membrane. Regardless, the electrical properties of the films stabilized after the first cycle of applied loading.

To further quantify the strain sensing properties of MWCNT-Pluronic thin films, the strain sensitivity (S) of each film can be calculated by:

$$S = \frac{\Delta R / R_0}{\Delta l / l_0} \tag{5}$$

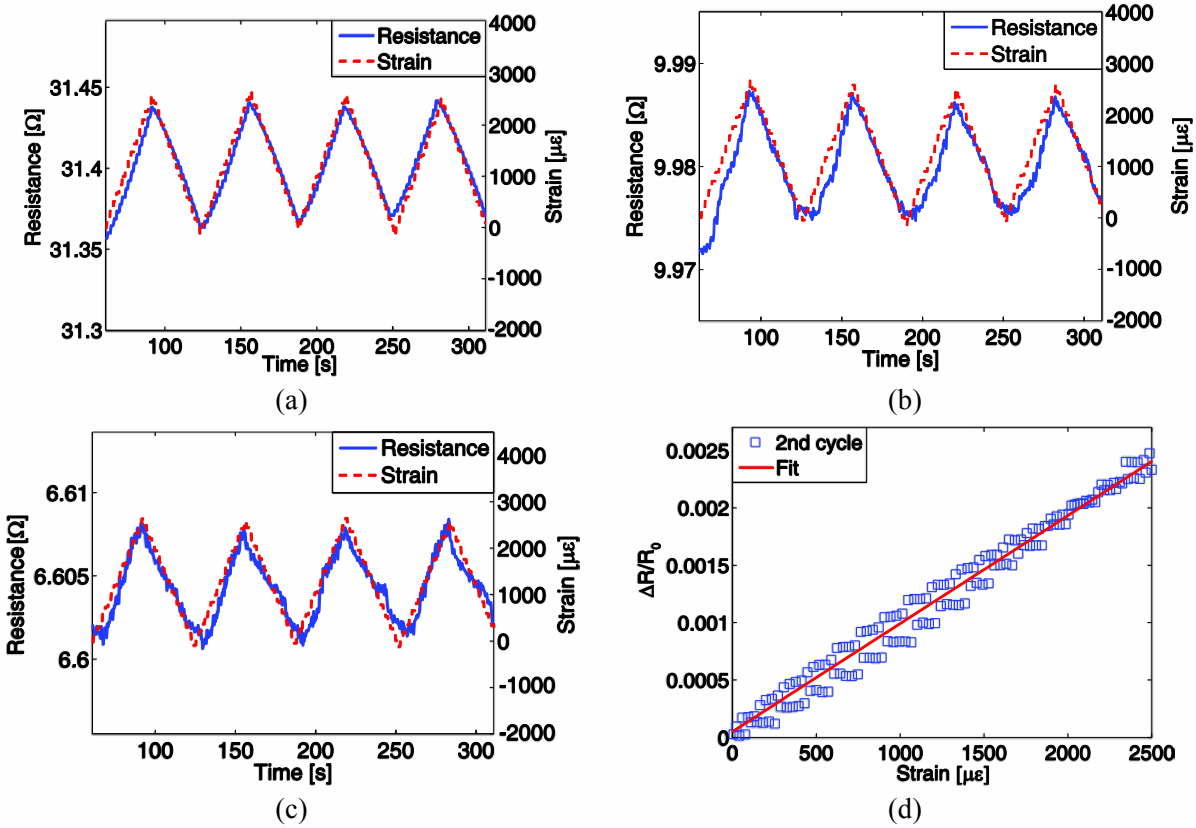

Figure 7. The electrical resistance responses of (a) 1, (b) 3, and (c) 5 mg/mL MWCNT-Pluronic strain sensors are overlaid with the corresponding applied strain time history. (d) The normalized change in resistance of a 1 mg/mL MWCNT-Pluronic strain sensor is plotted as a function of applied strains.

where ΔR is the change in resistance of the film at each applied strain state relative to the film's unstrained or nominal resistance (R_0), and Δl is the change in length of the film with respect to its initial gage length (l_0). In addition, $\Delta R/R_0$ can also be defined as the normalized change in resistance (R_{norm}), and $\Delta l/l_0$ is applied strain ($\Delta\varepsilon$). The strain sensitivity of each thin film specimen can then be estimated by fitting a linear least-squares regression line to the plot of R_{norm} versus $\Delta\varepsilon$, such as figure 7(d). In this study, S for each load cycle (*i.e.*, second to fifth cycles) was computed separately, and S for each film is reported as the average of the four cycles. For each MWCNT concentration, 10 different specimens were tested. Figure 8 summarize these results, and it can be seen that S decreased in an exponentially decaying fashion as the concentration of MWCNTs was increased from 0.25 to 5 mg/mL. This trend was consistent with other experimental and numerical studies [29, 40].

5. Numerical simulation results

By following the procedures outlined in Section 3, nanocomposite strain sensing properties of different models were simulated. First, uniaxial cyclic tensile-compressive strains to ± 10,000 με were applied (in 2,500 με increments). The coordinates were updated at each strain state, and the electrical resistance of the deformed model was calculated accordingly (Section 3). It should be mentioned that, before conducting strain sensing simulations, the percolation probability [60] of each model was calculated for $N = 250$. The percolation probability for $HR = 0$, 10, 20, and 30% were 60.4, 55.4, 51.4, and 29.4%, respectively. figure 9 shows the representative set of results corresponding to models of $N = 300$ and 800 ($HR = 20\%$). The

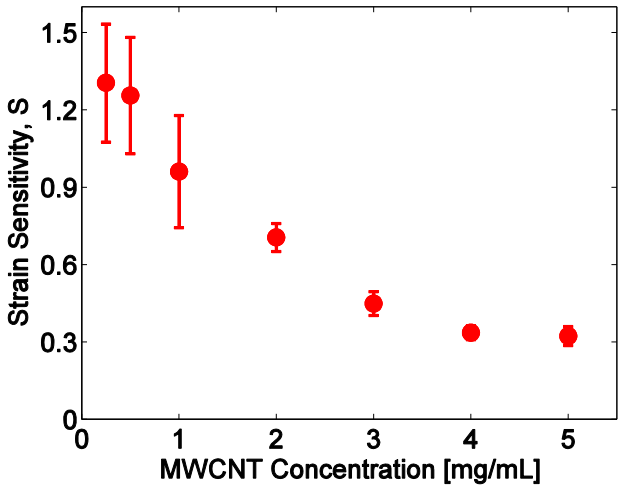

Figure 8. Strain sensitivities of MWCNT-Pluronic strain sensors and their error bars were obtained for buckypaper specimens fabricated using different MWCNT concentrations.

normalized change in resistance varied linearly in response to applied strains. To calculate the strain sensitivity of the model, a linear least-squares regression line was fitted to each dataset as before. The strain sensitivities of N = 300 and 800 were 1.14 and 0.61, respectively. Similar to the experimental results presented in Section 4, strain sensitivities were evaluated for models of different CNT densities (N). In addition, this study investigated the effects of variations in HR and CNT statistical length distributions on bulk film strain sensing properties.

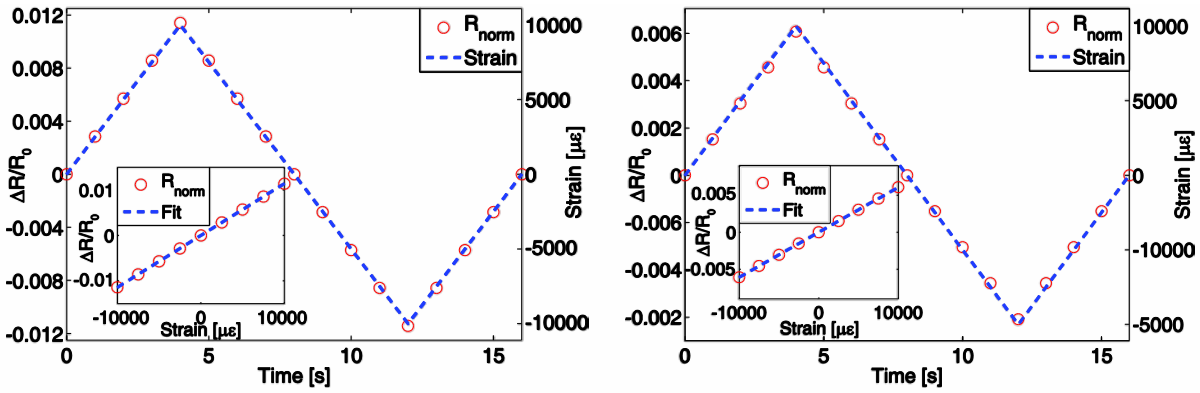

Figure 9. CNT-based nanocomposite models with (a) N = 300 and (b) N = 800 (HR = 20%) were subjected to a one-cycle tensile-compressive strain pattern to ±10,000 με, and their respective strain sensitivities were S = 1.14 and 0.61.

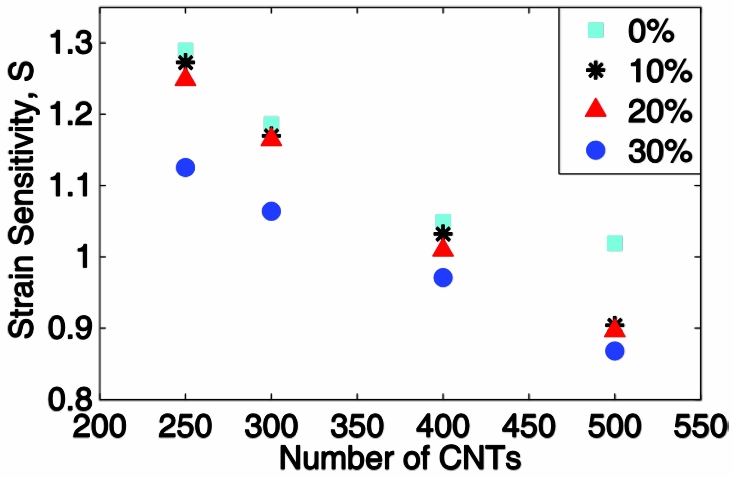

Figure 10. Strain sensitivities of nanocomposite models with different CNT densities (N) and shapes (HR = 0, 10, 20, and 30%) were computed.

The results are summarized in figures 10 and 11. Each data point corresponds to the average strain sensitivity calculated from 20 simulations (for each case). Both sets of results showed that strain sensitivity decreased as N increased. In particular, it can be seen from figure 10 that models with higher height ratios exhibited lower strain sensitivities as compared to those with lower HR. To be specific, when N = 250, the strain sensitivity for the HR = 30% case was 1.03, while that of HR = 0% (*i.e.*, CNTs were assumed to be straight elements) was 1.29. Figure 11 demonstrated that models that considered a Gaussian distribution of CNT lengths showed similar strain sensitivities than cases considering a fixed CNT length (*i.e.*, L_{CNT} = 1.904 μm), except at lower CNT densities and when the models were close to their percolation threshold (*i.e.*, N = 250 and 300). These numerical simulation results suggested that the geometrical features of dispersed CNTs and length distributions need to be considered for modeling nanocomposites, especially at lower CNT densities, since these effects influence the bulk film electrical properties.

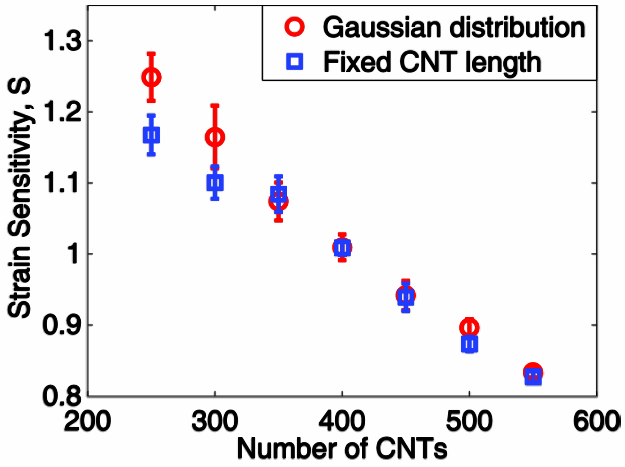

Figure 11. The strain sensitivities of nanocomposite models assembled using CNTs assumed to be of a fixed and a distribution of lengths were computed and compared.

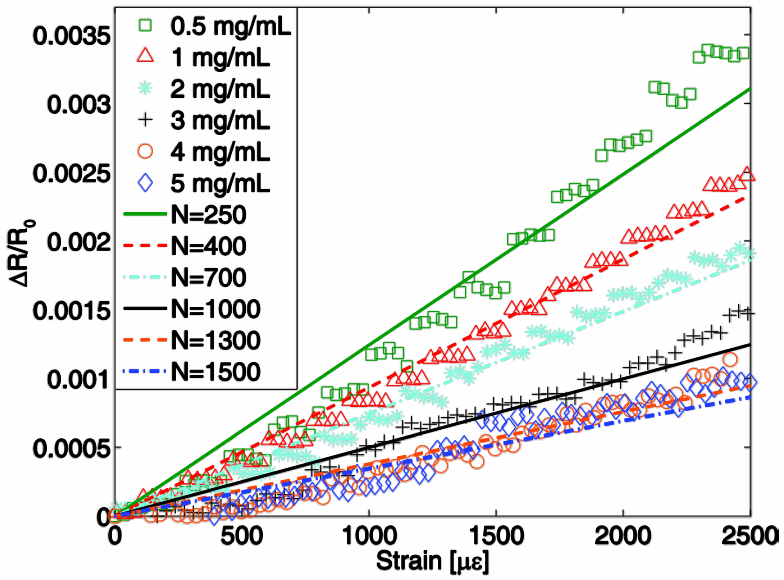

Figure 12. The experimental and numerical model strain sensing responses are compared by plotting the normalized change in resistance as a function of applied strains.

6. Comparison of experimental and numerical results

6.1. Strain sensing properties

From the results presented in Sections 4 and 5, both the MWCNT-Pluronic strain sensor test results and numerical models confirmed their linear piezoresistivity. Moreover, the model with HR = 20% showed similar strain sensing characteristics with the MWCNT-Pluronic test results. The normalized change in resistance of experimental tests results and numerical models with HR = 20% are plotted together with respect to applied tensile strains as shown in figure 12. Only the tensile test results are compared in figure 12, since it was not possible to apply compressive strains to the actual films as it would buckle the specimens. In figure 12, the numerical simulation results are presented as linear lines, whereas the experimental data points are plotted individually. Overall, figure 12 shows good matching between experimental and numerical results. It can also be observed that, as the density of MWCNTs increased, the slope of the lines and strain sensitivity decreased.

In figure 13, strain sensitivities of the models and MWCNT-Pluronic strain sensors are overlaid according to CNT density and MWCNT concentration in the film, respectively. Most of the strain sensitivity data from the models were generated from averages of 20 simulations, but due to computational demand and time, only 10 simulations were conducted for the N = 800 and 900 cases and five simulations for the 1,000 to 1,500 models. In addition to the average strain sensitivity, the error bars show the standard deviations for each CNT density case. In general, one can clearly see that the simulation results agreed with those obtained from strain sensing characterization tests conducted on actual MWCNT-Pluronic buckypaper specimens. For example, the strain sensitivity of 0.5 mg/mL MWCNT-Pluronic films (*i.e.*, S = 1.26) was approximately equal to the nanocomposite model with N = 250 (S = 1.25). These results suggest that the model proposed can be used to describe the strain sensing properties of MWCNT-Pluronic thin films.

6.2. Area ratio (AR)

Besides observing similarities between experiments and simulations, further validation of the 2D nanocomposite model can be performed by computing the area ratio (AR) of MWCNT-Pluronic buckypapers using SEM images. AR is defined as the ratio of MWCNT network area to the total area of the image and can be calculated using equation (6):

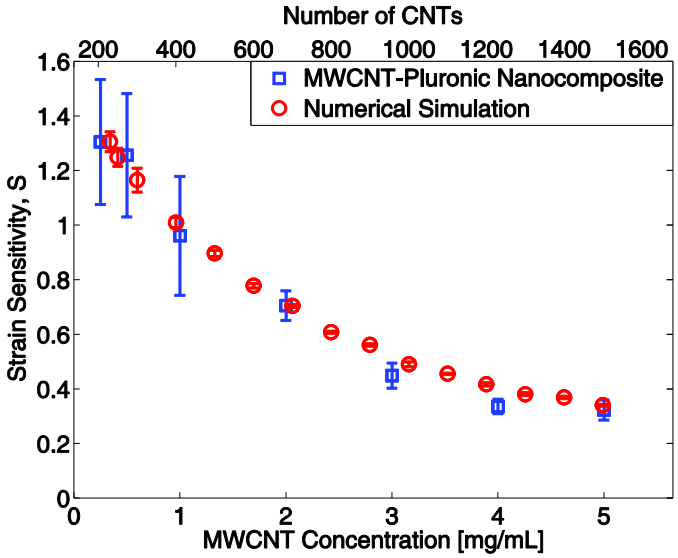

Figure 13. The strain sensitivities obtained from experimental tests and numerical simulations are compared for films with different MWCNT concentrations/densities.

$$AR = \frac{A_{CNTs}}{A_{total}} = \frac{N_1}{N_{pixel}} \tag{6}$$

where A_{CNTs} is the area occupied by MWCNTs, A_{total} is the total area of the image, N_1 is the number of pixels occupied by 1, and N_{pixel} is the number of pixels of the entire image. Essentially, AR computes the effective percentage of the 2D space that is occupied by the conductive MWCNTs. The area ratio is a simple and effective means for validation, because, ideally, AR for the numerical models should be comparable to those observed in experiments and in the actual films. However, it should be mentioned that there are limitations to this method. MWCNTs form a dense 3D percolated network in the films, and nanotubes do not only lie in a single plane. By virtue of using SEM images for computing AR, one is only considering a planar view of the complex network. However, the model presented in this study is an effective simplified numerical model that was derived from 2D AFM and SEM images of individual nanotubes. In that regard, the initial inputs to the numerical model (*e.g.*, statistical length distributions of nanotubes) already considers the non-planar orientation of MWCNTs.

The first step is to compute AR of actual MWCNT-Pluronic thin films. First, SEM images of MWCNT-Pluronic buckypapers were obtained (figure 14(a)) using a Zeiss SIGMA 500 with an accelerating voltage of 3 kV. Since the interest of this study was the surface topography of MWCNT-Pluronic buckypapers, a secondary electron detector was used. Second, the SEM image in RGB format was imported to MATLAB and converted to gray-scale, using built-in functions available from MATLAB's image processing toolbox. A histogram of the image was used to observe the image pixel intensity distribution. Since the histogram of gray-scale SEM images tended to show that intensity of the image was biased toward the dark end, image contrast was enhanced using the histogram equalization method (figure 14(b)). Third, to define the edge of MWCNTs, the enhanced images in gray-scale were converted into binary black-and-white images (figure 14(c)) by determining pixel intensity ranges (*i.e.*, region of interest). It should be noted that, in the gray-scale image, a translucent interface was observed near the edges of MWCNTs, which was considered as polymer (*i.e.*, Pluronic) covering the MWCNTs [61]. In the binary image such as figure 14(c), the white area (*i.e.*, 1 in binary representation) was considered as MWCNTs, whereas black was regarded as the polymer matrix or vacant region.

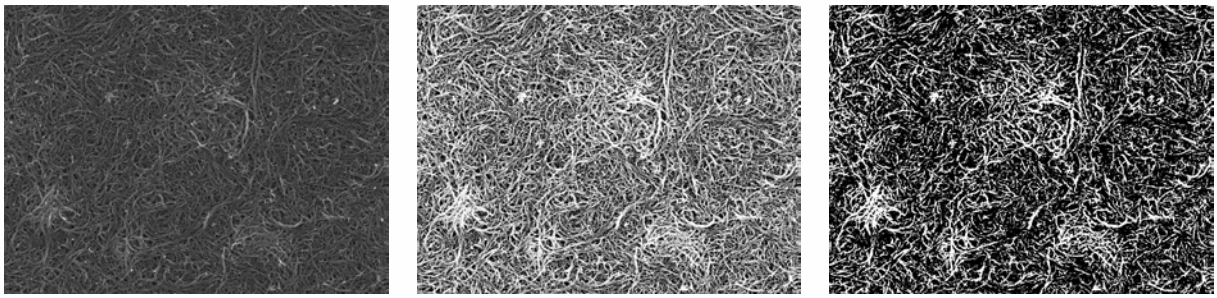

(a) (b) (c)

Figure 14. The area ratio of MWCNT-Pluronic nanocomposites was determined by following three steps: (a) acquire SEM image; (b) enhance image; and (c) convert enhanced image into a binary image.

SEM images of four different MWCNT concentrations (2, 3, 4, and 5 mg/mL) are shown in figure 15. SEM images of lower MWCNT concentrations (0.25 to 1 mg/mL) were excluded, since MWCNT boundaries were less clear, and the images were also affected by charging effect. In this work, a conductive coating was not used to preserve the pristine nanocomposite surface. It can be seen in figure 15 that, as MWCNT concentration increased, more MWCNTs were distributed and less voids are present. Furthermore, the film's surface topography became more nonuniform. For example, by comparing 2 and 3 mg/mL SEM

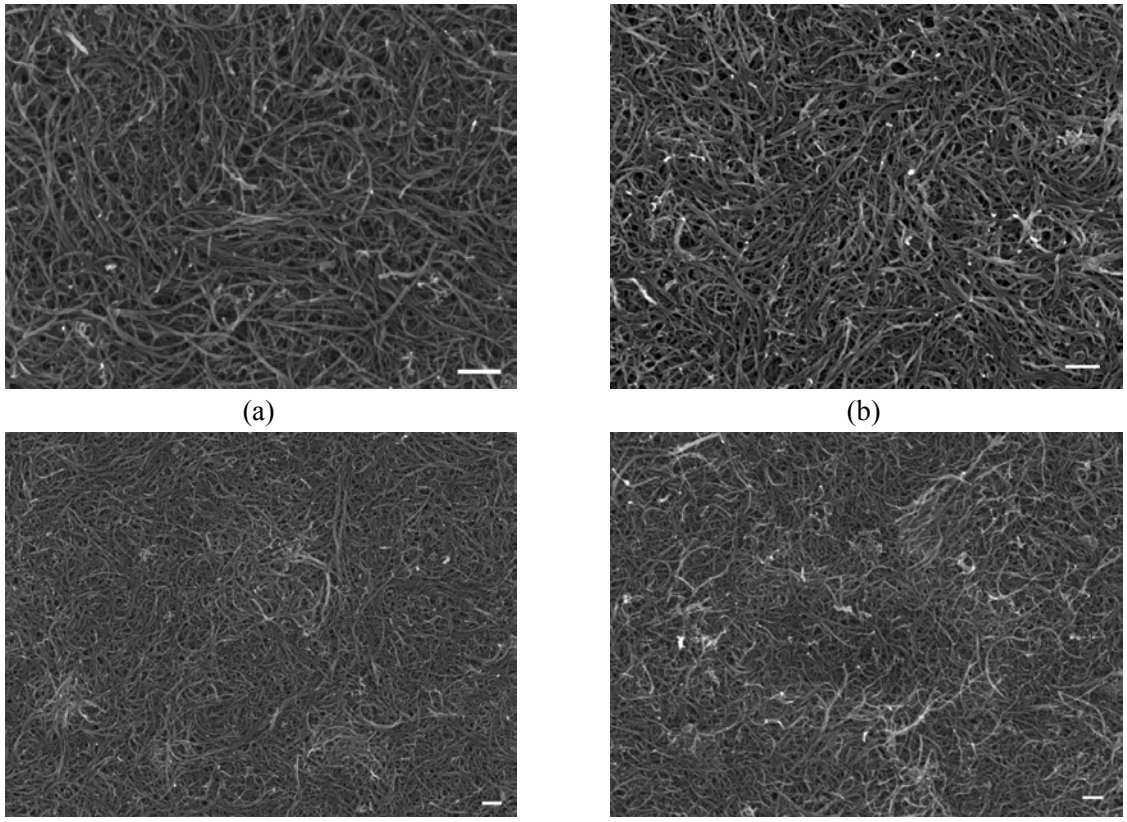

(a) (b)

(c) (d)

Figure 15. SEM images of MWCNT-Pluronic thin films with (a) 2, (b) 3, (c) 4, and (d) 5 mg/mL concentrations are shown. The white scale bar represents 200 nm.

images (figure 15(a)-(b)) to 4 and 5 mg/mL ones (figure 15(c)-(d)), it can be seen that there are regions with clusters of dispersed MWCNTs situated higher than other regions of the film. This, however, was not an issue and was considered during image analysis by adjusting pixel intensity ranges when the grayscale images were converted to binary images.

Similarly, the area ratio of the nanocomposite numerical model was also evaluated. Although the diameter of CNTs was not specified in the model during simulations, one can still consider CNT diameter during image analysis. An SEM image of MWCNT-Pluronic nanocomposite was used to define the average diameter for as-deposited MWCNTs. Diameter was determined by measuring the two edge boundaries of an MWCNT in the SEM image. Most diameter measurements ranged from 15 to 25 nm, so an average diameter of 20 nm was assumed and applied to the model. Then, the RGB image of the numerical model was saved (after model generation) and processed in the same manner as the aforementioned experimental case; the only difference was that image enhancement was not required.

Since it was demonstrated in figure 13 that the strain sensitivity of 2 mg/mL MWCNT-Pluronic strain sensor ($S = 0.71$) was similar to that of the $N = 700$ model ($S = 0.70$), area ratios of numerical models with $N \geq 700$ were calculated and compared, following the aforementioned procedures. In figure 16, area ratio results of MWCNT-Pluronic strain sensor experimental tests and numerical models were summarized. Similar to the strain sensitivity results, area ratios of MWCNT-Pluronic buckypapers were comparable to those computed for the numerical models. For example, AR for 3 mg/mL buckypaper was 0.262 and was similar to that of the corresponding $N = 1{,}000$ model ($AR = 0.242$). It should be noted that the size of the model space is irrelevant, since AR is always normalized with respect to the dimensions. Despite the favorable area ratio results, AR for the model was slightly lower than those computed from experimental SEM images. A possible reason could be due to the inherent nature of imaging, where the SEM image attempts to capture everything in its 3D view but flattened to form a 2D image. Therefore, nanotubes near the surface appeared to be brighter and larger compared to nanotubes located subsurface. During image analysis, the brighter area with high intensity was regarded as MWCNTs, the polymer close to the surface could appear with the same shade of gray as compared to nanotubes in a lower plane [62]. In addition, another source of error could be the assumption of a constant CNT diameter for the numerical models.

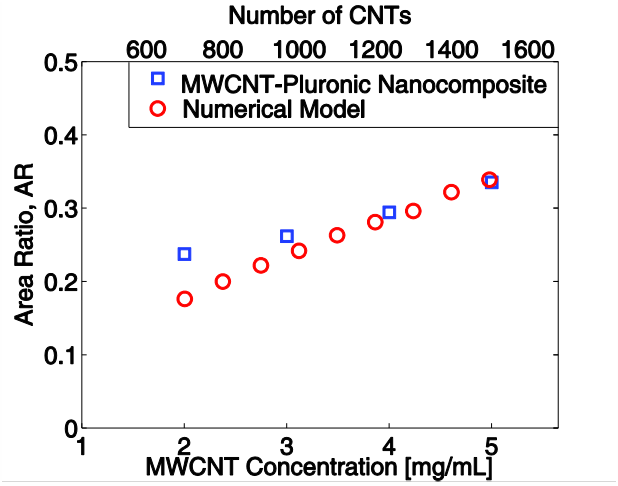

Figure 16. The area ratios of MWCNT-Pluronic nanocomposites and numerical models were evaluated and compared.

7. Conclusions

The objective of this study was to characterize the strain sensing properties of MWCNT-Pluronic thin films and to compare experimental and numerical modeling results. First, MWCNT-Pluronic buckypaper specimens were fabricated by vacuum filtration, and seven different MWCNT concentration sample sets were prepared. The films' unstrained electrical properties were measured, and they were also subjected to electromechanical tests. Second, a 2D nanocomposite percolation-based model was derived, taking into account the kinked shape CNTs and statistical length distributions observed from SEM images of MWCNT-Pluronic buckypapers. The model's nominal electrical properties, as well as at different applied strain states, were computed by constructing a conductance matrix of the CNT network and then applying Kirchhoff's current law and the conductance version of Ohm's law. Lastly, the experimental and numerical simulation results were compared. Both the model and the experimental results revealed the linear piezoresistive properties of the nanocomposites. Furthermore, both results showed that strain sensitivity decreased as CNT density was increased. Not only were these trends the same, the values for strain sensitivities were also similar, thereby suggesting that the models accurately described the electromechanical properties of the films. To further validate the nanocomposite model, an area ratio calculation was defined. Image processing was employed to compute the area ratio of MWCNT-Pluronic buckypapers (using SEM images), as well as for the numerical models. The area ratios between experiments and the models were comparable, thereby successfully validating that the models' physical and electromechanical properties represented that of the actual buckypapers fabricated.

Acknowledgements

This research was supported by the U.S. National Science Foundation under grant number CMMI CAREER 1253564. Additional Support was also provided by the Jacobs School of Engineering, University of California-San Diego. The authors also acknowledge the collaboration of Prof. Yuan-Sen Yang in the Department of Civil Engineering at the National Taipei University of Technology (Taiwan).

References

[1] Suri K, Annapoorni S, Sarkar A K and Tandon R P 2002 Gas and humidity sensors based on iron oxide-polypyrrole nanocomposites *Sens. Actuat B: Chem.* **81** 277-82

[2] Cui Y, Zhong Z, Wang D, Wang W U and Lieber C M 2003 High performance silicon nanowire field effect transistors *Nano Lett.* **3** 149-52

[3] Iijima S 1991 Helical microtubules of graphitic carbon *Nature* **354** 56-8

[4] Rao C N R, Sood A K, Subrahmanyam K S and Govindaraj A 2009 Graphene: the new two-dimensional nanomaterial *Angew. Chem. Int. Ed.* **48** 7752-77

[5] Lapshin R V 2016 STM observation of a box-shaped graphene nanostructure appeared after mechanical cleavage of pyrolytic graphite *Appl. Surf. Sci.* **360** 451-60

[6] Bandaru P R 2007 Electrical properties and applications of carbon nanotube structures *J. Nanosci. Nanotechnol.* **7** 1-29

[7] Shi J, Zhu Y, Zhang X, Baeyens W R G and García-Campaña A M 2004 Recent developments in nanomaterial optical sensors *TrAC Trends Anal. Chem.* **23** 351-60

[8] Lu Y, Yin Y, Mayers B T and Xia Y 2002 Modifying the surface properties of superparamagnetic iron oxide nanoparticles through a sol−gel approach *Nano Lett.* **2** 183-6

[9] Bhatia R, Prasad V and Menon R 2010 Characterization, electrical percolation and magnetization studies of polystyrene/multiwall carbon nanotube composite films *Mater. Sci. Eng. B* **175** 189-94

[10] Baughman R H, Zakhidov A A and de Heer W A 2002 Carbon nanotubes-the route toward applications *Science* **297** 787-92

[11] Ebbesen T W, Lezec H J, Hiura H, Bennett J W, Ghaemi H F and Thio T 1996 Electrical conductivity of individual carbon nanotubes *Nature* **382** 54-6

[12] Treacy M M J, Ebbesen T W and Gibson J M 1996 Exceptionally high Young's modulus observed for individual carbon nanotubes *Nature* **381** 678-80

[13] Yu M-F, Lourie O, Dyer M J, Moloni K, Kelly T F and Ruoff R S 2000 Strength and breaking mechanism of multiwalled carbon nanotubes under tensile load *Science* **287** 637-40
[14] Tombler T W, Zhou C, Alexseyev L, Kong J, Dai H, Liu L, Jayanthi C S, Tang M and Wu S-Y 2000 Reversible electromechanical characteristics of carbon nanotubes under local-probe manipulation *Nature* **405** 769-72
[15] Ruan S L, Gao P, Yang X G and Yu T X 2003 Toughening high performance ultrahigh molecular weight polyethylene using multiwalled carbon nanotubes *Polymer* **44** 5643-54
[16] Gojny F H, Wichmann M H G, Fiedler B and Schulte K 2005 Influence of different carbon nanotubes on the mechanical properties of epoxy matrix composites – A comparative study *Compos. Sci. Technol.* **65** 2300-13
[17] Kim Y J *et al* 2005 Hybridization of oxidized MWNT and silver powder in polyurethane matrix for electromagnetic interference shielding application *IEEE Trans. Electromagn. Compat.* **47** 872-9
[18] Sandler J K W, Kirk J E, Kinloch I A, Shaffer M S P and Windle A H 2003 Ultra-low electrical percolation threshold in carbon-nanotube-epoxy composites *Polymer* **44** 5893-9
[19] Martin C A, Sandler J K W, Shaffer M S P, Schwarz M K, Bauhofer W, Schulte K and Windle A H 2004 Formation of percolating networks in multi-wall carbon-nanotube–epoxy composites *Compos. Sci. Technol.* **64** 2309-16
[20] Biercuk M J, Llaguno M C, Radosavljevic M, Hyun J K, Johnson A T and Fischer J E 2002 Carbon nanotube composites for thermal management *Appl. Phys. Lett.* **80** 2767-9
[21] Obitayo W and Liu T 2012 A review: carbon nanotube-based piezoresistive strain sensors *Journal of Sensors* **2012** 1-15
[22] Alamusi, Hu N, Fukunaga H, Atobe S, Liu Y and Li J 2011 Piezoresistive strain sensors made from carbon nanotubes based polymer nanocomposites *Sensors* **11** 10691-723
[23] Lee B M, Gupta S, Loh K J and Nagarajaiah S 2016 *Innovative developments of advanced multifunctional nanocomposites in civil and structural engineering,* ed K J Loh and S Nagarajaiah (Amsterdam: Elsevier) pp 303-26
[24] Zhang Z, Wei H, Liu Y and Leng J 2015 Self-sensing properties of smart composite based on embedded buckypaper layer *Struct. Health Monit.* **14** 127-36
[25] Loh K J, Kim J, Lynch J P, Kam N W S and Kotov N A 2007 Multifunctional layer-by-layer carbon nanotube–polyelectrolyte thin films for strain and corrosion sensing *Smart Mater. Struct.* **16** 429-38
[26] Mortensen L P, Ryu D, Zhao Y and Loh K J 2013 Rapid assembly of multifunctional thin film sensors for wind turbine blade monitoring *Key Eng. Mater.* **569** 515-22
[27] Kang J H, Park C, Scholl J A, Brazin A H, Holloway N M, High J W, Lowther S E and Harrison J S 2009 Piezoresistive characteristics of single wall carbon nanotube/polyimide nanocomposites *J. Polym. Sci. Part B* **47** 1635–6
[28] Kanoun O, Müller C, Benchirouf A, Sanli A, Trong Nghia D, Al-Hamry A, Lei B, Gerlach C and Bouhamed A 2014 Flexible carbon nanotube films for high performance strain sensors *Sensors* **14** 10042-71
[29] Hu N, Karube Y, Arai M, Watanabe T, Yan C, Li Y, Liu Y and Fukunaga H 2010 Investigation on sensitivity of a polymer/carbon nanotube composite strain sensor *Carbon* **48** 680-7
[30] Kordás K *et al* 2006 Inkjet printing of electrically conductive patterns of carbon nanotubes *Small* **2** 1021-5
[31] Hu L, Hecht D S and Grüner G 2010 Carbon nanotube thin films: fabrication, properties, and applications *Chem. Rev.* **110** 5790-844
[32] Loh K J and Azhari F 2012 Recent advances in skin-inspired sensors enabled by nanotechnology *JOM* **64** 793-801
[33] Rahman R, Soltanian S and Servati P 2016 Coupled effects of film thickness and filler length on conductivity and strain sensitivity of carbon nanotube/polymer composite thin films *IEEE Sensors J.* **16** 77-87

[34] Loh K J, Lynch J P, Shim B S and Kotov N A 2008 Tailoring piezoresistive sensitivity of multilayer carbon nanotube composite strain sensors *J. Intell. Mater. Syst. Struct.* **19** 747-64
[35] Yamada T, Hayamizu Y, Yamamoto Y, Yomogida Y, Izadi-Najafabadi A, Futaba D N and Hata K 2011 A stretchable carbon nanotube strain sensor for human-motion detection *Nat. Nanotechnol.* **6** 296-301
[36] Zhao Y, Viechtbauer C, Loh K J and Schagerl M 2015 Enhancing the strain sensitivity of carbon nanotube-polymer thin films for damage detection and structural monitoring *Proc. Advanced Smart Materials and Smart Structures Technology (Urbana-Champaign, August 1-2)*
[37] Hu N, Karube Y, Yan C, Masuda Z and Fukunaga H 2008 Tunneling effect in a polymer/carbon nanotube nanocomposite strain sensor *Acta. Mater.* **56** 2929-36
[38] Rahman R and Servati P 2012 Effects of inter-tube distance and alignment on tunnelling resistance and strain sensitivity of nanotube/polymer composite films *Nanotechnology* **23** 055703
[39] Wang Z and Ye X 2013 A numerical investigation on piezoresistive behaviour of carbon nanotube/polymer composites: mechanism and optimizing principle *Nanotechnology* **24** 265704
[40] Amini A and Bahreyni B 2012 Behavioral model for electrical response and strain sensitivity of nanotube-based nanocomposite materials *J. Vac. Sci. Technol., B* **30** 022001
[41] Lee B M and Loh K J 2015 A 2D percolation-based model for characterizing the piezoresistivity of carbon nanotube-based films *J. Mater. Sci.* **50** 2973-83
[42] Dharap P, Li Z, Nagarajaiah S and Barrera E V 2004 Nanotube film based on single-wall carbon nanotubes for strain sensing *Nanotechnology* **15** 379-82
[43] Vaisman L, Wagner H D and Marom G 2006 The role of surfactants in dispersion of carbon nanotubes *Adv. Colloid Interface Sci.* **128–130** 37-46
[44] Shvartzman-Cohen R, Florent M, Goldfarb D, Szleifer I and Yerushalmi-Rozen R 2008 Aggregation and self-assembly of amphiphilic block copolymers in aqueous dispersions of carbon nanotubes *Langmuir* **24** 4625-32
[45] Pop E, Mann D, Wang Q, Goodson K and Dai H 2006 Thermal conductance of an individual single-wall carbon nanotube above room temperature *Nano Lett.* **6** 96-100
[46] Chen R J, Franklin N R, Kong J, Cao J, Tombler T W, Zhang Y and Dai H 2001 Molecular photodesorption from single-walled carbon nanotubes *Appl. Phys. Lett.* **79** 2258-60
[47] Yu H, Cao T, Zhou L, Gu E, Yu D and Jiang D 2006 Layer-by-Layer assembly and humidity sensitive behavior of poly(ethyleneimine)/multiwall carbon nanotube composite films *Sens. Actuat B: Chem.* **119** 512-5
[48] Dalmas F, Dendievel R, Chazeau L, Cavaillé J-Y and Gauthier C 2006 Carbon nanotube-filled polymer composites. Numerical simulation of electrical conductivity in three-dimensional entangled fibrous networks *Acta. Mater.* **54** 2923-31
[49] Li C and Chou T-W 2007 Continuum percolation of nanocomposites with fillers of arbitrary shapes *Appl. Phys. Lett.* **90** 174108
[50] Yi Y B, Berhan L and Sastry A M 2004 Statistical geometry of random fibrous networks, revisited: Waviness, dimensionality, and percolation *J. Appl. Phys.* **96** 1318-27
[51] Li C, Thostenson E T and Chou T-W 2008 Effect of nanotube waviness on the electrical conductivity of carbon nanotube-based composites *Compos. Sci. Technol.* **68** 1445-52
[52] Berhan L and Sastry A M 2007 Modeling percolation in high-aspect-ratio fiber systems. II. The effect of waviness on the percolation onset *Physical Review E* **75** 041121
[53] Lee B M, Loh K J and Yang Y-S 2016 Carbon nanotube thin film strain sensor models assembled using nano- and micro-scale imaging *Computational Mechanics* Accepted
[54] Behnam A and Ural A 2007 Computational study of geometry-dependent resistivity scaling in single-walled carbon nanotube films *Phys. Rev. B* **75** 125432
[55] Javey A and Kong J 2009 *Carbon nanotube electronics* (New York: Springer)
[56] Fuhrer M S *et al* 2000 Crossed nanotube junctions *Science* **288** 494-7
[57] Fuhrer M S, Lim A K L, Shih L, Varadarajan U, Zettl A and McEuen P L 2000 Transport through crossed nanotubes *Physica E* **6** 868-71

[58] Cullinan M A and Culpepper M L 2010 Carbon nanotubes as piezoresistive microelectromechanical sensors: Theory and experiment *Phys. Rev. B* **82** 115428
[59] Lee B M, Wang L and Loh K J 2015 Characterization of carbon nanotube strain sensors using experimental tests and percolation modeling *Proc. 10th Int. Workshop on Structural Health Monitoring (Stanford, CA, September 1-3)*
[60] Zeng X, Xu X, Shenai P M, Kovalev E, Baudot C, Mathews N and Zhao Y 2011 Characteristics of the electrical percolation in carbon nanotubes/polymer nanocomposites *J. Phys. Chem. C* **115** 21685-90
[61] Li W, Buschhorn S T, Schulte K and Bauhofer W 2011 The imaging mechanism, imaging depth, and parameters influencing the visibility of carbon nanotubes in a polymer matrix using an SEM *Carbon* **49** 1955-64
[62] Zhao M *et al* 2015 New insights into subsurface imaging of carbon nanotubes in polymer composites via scanning electron microscopy *Nanotechnology* **26** 085703